Numerical modeling of multilayer film coextrusion with experimental validation

Champion, James; Looney, M. Kieran; Simmons, Mark

DOI:
10.1002/pen.24022

Document Version
Publisher's PDF, also known as Version of record

Citation for published version (Harvard):
Champion, J, Looney, MK & Simmons, MJH 2015, 'Numerical modeling of multilayer film coextrusion with experimental validation', Polymer Engineering and Science, vol. 55, no. 8, pp. 1829–1842. https://doi.org/10.1002/pen.24022

Numerical Modeling of Multilayer Film Coextrusion With Experimental Validation

James Champion,[1,2] M. Kieran Looney,[1] Mark J.H. Simmons[2]
[1] *DuPont Teijin Films U.K. Limited, The Wilton Centre, Redcar, TS10 4RF, UK*
[2] *School of Chemical Engineering, University of Birmingham, Edgbaston, B15 2TT, UK*

Computational fluid dynamics (CFD) using a finite volume technique and the volume of fluid method of interface tracking is used to model the production of polyester-based multilayered films via coextrusion. Experimental methods encompass both overall flow validation and secondary layer thickness validation. The interpretation of frozen die plugs and layer thickness measurements of unstretched cast films using chloroform washing are used for overall flow validation. For secondary layer thickness validation, layer thickness measurements via both white light interferometry and chloroform washing of stretched final film samples are presented. Good agreement between CFD results and both die plug structures and layer thicknesses from chloroform washing of cast film is observed. When investigating final film samples, there is a good agreement between CFD and white light interferometry, based on individual layer thickness calculations. However, the layer thicknesses from chloroform washing of final films are lower than those obtained from both CFD and white light interferometry. This is attributed to partial crystallization of the thinner polymer at the interface after stretching and heating the film. **POLYM. ENG. SCI., 00:000–000, 2014.** **© 2014 The Authors. Polymer Engineering & Science published by Wiley Periodicals, Inc. on behalf of Society of Plastics Engineers**

INTRODUCTION

Multilayer polymer film coextrusion is defined as two or more separately extruded polymer melt streams coming together to form a single stratified structure with multiple layers [1–4]. In the coextrusion process, the different melt layers must remain distinct but well bonded (or compatible) when in contact [5, 6]. Assuming that a desirable final coextrusion structure is obtained, coextrusion can combine the properties of different polymers into a single structure with improved features [1–4, 7]. There are many aspects that one must consider to obtain a successful coextruded product. These include both the flow properties of the polymer melts involved and details of the coextrusion hardware used [8].

DuPont Teijin Films (DTF) uses coextrusion to produce biaxially oriented polyester-based multilayered films on a commercial scale. The individual layers of a DTF multilayered film are based on either polyethylene terephthalate (PET) or polyethylene naphthalate (PEN). The main market areas for such multilayered films include flexible electronics, photovoltaics, cards, and food packaging. Typical DTF multilayered films are shown in cross-section in Fig. 1, where A (blue), B (pink), and C (yellow) represent different polymer layers. The multilayered films increase in complexity when moving from Fig. 1a–e. Figure 1a depicts an AB structured film, as investigated numerically and experimentally in this article.

The multilayered films in Fig. 1 are produced when different polymers are extruded, producing separate polymer melt streams. These streams then come together for the first time in either an injector (or feed) block linked to a die or a multimanifold die [1, 4, 5, 8–15]. A thin, unified melt curtain sheet exits the die, which is then rapidly cooled by a casting drum before being stretched in both the machine and transverse directions, producing a biaxially oriented *final film* [5]. Any film sample that has been cooled but not stretched is referred to as cast film. It is often desirable to produce a film with clear edges (Fig. 1a and b). This is when the thinner secondary layers are not present at the edges of the film. The main advantage of attaining clear edges is that trimming of these film edges during production leads to single-component recycling of the main primary polymer.

The multilayered films in Fig. 1 are idealized; there is tight individual layer thickness control across the film widths and there is a linear interface between the different layers. This is not always obtainable and certain coextrusion issues can have a negative impact on the final product performance [3]. Both viscous and elastic melt property differences can lead to an unwanted nonlinear interface, which would have deleterious effects upon the optical, physical, and mechanical film properties [15, 16]. Such interfacial irregularity can be either spatial (caused by viscous effects) or temporal (elastic effects). At the shear rates in the film production process ($\dot{\gamma} < 150\ s^{-1}$ for the hardware and polymers used in this study), polyester melt flows are considered Newtonian and inelastic [17–20]. The analysis presented in this article therefore considers only viscous effects in polymer coextrusion and ignores elastic effects. Further justification of the Newtonian, inelastic assumption made for the PET polymers is shown in the materials section.

When the polymer melts are flowing as a unified structure, the lower viscosity polymer moves to the geometry walls and flows round the higher viscosity polymer(s), producing a curved final interface [1, 8, 10, 21, 22]. This phenomenon is known as interfacial curvature and occurs because the higher viscosity material seeks the area of lowest resistance away from the geometry walls, which is energetically more favorable. The more viscous fluid tends to push into the less viscous one to minimize viscous dissipation [21, 23, 24]. Interfacial curvature

Correspondence to: James Champion; e-mail: james.champion@gbr.dupont.com
Contract grant sponsors: Engineering and Physical Sciences Research Council (EPSRC) and DuPont Teijin Films in the Industrial Doctoral Centre in Formulation Engineering, School of Chemical Engineering, University of Birmingham (Engineering Doctorate Studentship to J.C.).
DOI 10.1002/pen.24022
Published online in Wiley Online Library (wileyonlinelibrary.com).

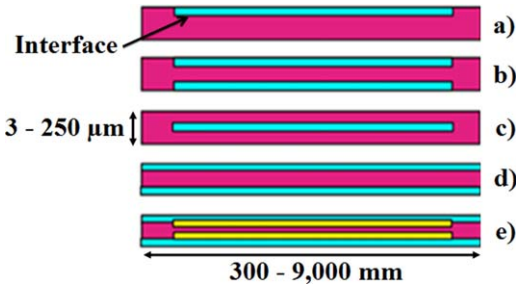

FIG. 1. Typical DTF multilayered film cross-sectional structures: (a) AB with clear edges, (b) ABA with clear edges, (c) BAB encapsulated core, (d) ABA without clear edges, and (e) ACBCA with C clear of edges. Diagram obtained from the internal DTF database. [Color figure can be viewed in the online issue, which is available at wileyonlinelibrary.com.]

can lead to full encapsulation of the lower viscosity polymer around the higher viscosity one(s) for wide geometries or large viscosity ratios. Everage [25] and to a lesser extent Williams [26] showed theoretically that full encapsulation is the most energetically preferred interfacial configuration as it has the lowest energy loss overall.

Work on viscous effects in polymer coextrusion has been ongoing since the 1970s. This early work focused on experimental and theoretical analysis of injector block rather than multimanifold die coextrusion. In the injector block approach, as modeled in this article, the separate polymer melt streams come together to form a unified melt structure. This melt composition then enters a die, where it is spread across the die width and then converted into a uniformly thin melt curtain [1, 8, 10]. In the more controlled, but less flexible multi-manifold die configuration, both layers are spread independently before merging to form the melt curtain [12, 13].

Some of the early fundamental publications on viscous effects include those by Han [27], Southern and Ballman [28, 29], and Lee and White [30]. Han [27] demonstrated via experiment full encapsulation of low density polyethylene (LDPE) around polystyrene (PS) at high LDPE flow rates. Southern and Ballman [28, 29] experimentally demonstrated a reversal of the direction of interfacial curvature for two PS resins at a critical wall shear rate value ($\dot{\gamma}_w$) of 14.9 s^{-1}. LDPE and PS melt flows exhibit a degree of shear thinning and work in Refs. [27–30] demonstrates the effect of shear rate on the interfacial configuration. Shear effects on viscosity are not considered in this article due to the Newtonian nature of polyester melt flows but they are important when studying polymer coextrusion as a whole. A detailed summary of the important early findings in polymer coextrusion is given by Han [31].

More recent publications have been on experimental measurement and numerical modeling of polymer coextrusion. Recent experimental studies further investigated viscous encapsulation. The degree of interfacial curvature, which leads to encapsulation, increases with both increasing viscosity ratios and wider geometries [1, 21]. It is stated in [23] that under standard conditions, encapsulation occurs after 100D, where D is the pipe diameter. Differences in the elasticity of the melt layers can also affect the coextruded structure and lead to elastic-based layer deformation and encapsulation [1, 8, 9, 14, 22, 23, 32, 33]. In elastic encapsulation, the more elastic fluid tends to push into the less elastic one [14, 30]. For further information on elastic effects in polymer coextrusion (not described in this study), the reader is directed toward Refs. [1, 3, 13, 14, 21, 23], and [32–37]. It is stated in Ref. [23] that the viscous rather than elastic contrast between different polymer melt layers is the more dominant factor regarding encapsulation.

Dooley [1] and Dooley and Rudolph [38] showed encapsulation of a lower viscosity PS resin around a higher viscosity PS resin in a laboratory scale injector block and die. In these works, the thicker primary polymer was dyed using carbon black, allowing for easy visualization of the two layers when the die was cooled and the consequent die plug extracted. A similar die plug analysis on a DTF die is demonstrated in the experimental section of this article.

Dooley [39, 40] and Dooley et al. [41] used a novel experimental method to measure the rheology of coextruded structures based on either PE or LDPE. An experiment was designed, allowing for the rheology of fully encapsulated melt structures to be measured. This multilayer rheology was then compared with the individual melt phases making up the structure, based on their shear thinning behavior. A main finding in Refs. [39–41] was that the rheology of the fully encapsulated form was similar to the skin layer rheology and this did not change even in four layered structures. This observation occurs because in fully encapsulated form only the secondary layer is at the walls and the shear rate is highest here. This explains why changing the secondary layer thickness does not alter either the pressure drop or the edge thickness profile during extrusion.

With the increase in computer power and software packages available, numerical methods have been used since the 1980s to study the viscous effects of polymer coextrusion. The majority of numerical coextrusion investigations use a finite element computational fluid dynamics (CFD) technique. A common theme, as shown by Mavridis et al. [42], Karagiannis et al. [43], Gifford [44], and Gupta [45, 46] is that the degree of numerically predicted interfacial curvature is less than that predicted experimentally using similar conditions in publications such as Refs. [28] and [29]. This disagreement is attributed to the wall conditions set in the CFD models. Full encapsulation has never before been modeled in a full three dimensional (3D) simulation.

Sornberger et al. [47] used a simplified iterative finite difference approach to model polymer coextrusion. Two 2D die geometries were modeled after linking to an injector block: A centre fed die and a slight variant of this. The authors show that viscosity-based interfacial curvature occurs and is mainly apparent in the die body rather than the lips. The authors also demonstrate good agreement between numerical and experimental work. However, the model is of a simplified nature and is unable to represent full encapsulation.

Unidirectional, 2D coextrusion was modeled by Karagiannis et al. [48]. A finite element, evolving mesh was used. As expected, it was found that interfacial curvature increases with increasing viscosity and (less viscous : more viscous fluid) flow rate ratios. Full encapsulation was shown numerically for large viscosity ratios. In Ref. [48], such encapsulation is attributed to the minimum viscous dissipation principle as shown in Refs. [25] and [26]. Three dimensional studies investigating the viscosity and flow rate ratios were conducted by Gifford [44]. Similar results to those in Ref. [48] were found, although full encapsulation was not predicted.

A problem with finite element-based CFD modeling is in the discontinuity of the viscous stress and pressure at the interface

 DOI 10.1002/pen

[39]. This problem was investigated in Refs. [42] and [43] by having nodes either side of the interface that the pressure and velocity are solved on, known as the double node method. Both publications apply 3D finite element modeling to simplified injector block geometries. In each case, there is good qualitative but poor quantitative agreements with the experimental results in Refs. [28] and [29]. In particular, the degree of interfacial curvature predicted numerically was less than that observed experimentally. Mitsoulis and Heng [24] also used the double node technique to simulate inelastic polymer coextrusion. Pressure gradient discrepancies were found to exist between the numerical results in Ref. [24] and the experimental data presented by Han [49].

One of the suggested reasons in Ref. [43] for the slightly ambiguous numerical and experimental correlation is the numerical treatment of contact lines. A fluid/fluid/solid contact line is defined as a region between the interface and the wall [43, 50]. In finite element simulations a no-slip condition (zero wall velocity) can give an unrealistic multivalued velocity. Also, there is infinite pressure at the three phase contact point since the no-slip condition cannot hold if this contact point is moving. In Ref. [43], a slight variant of the no-slip contact line was used. Torres et al. [50] extended this to introduce a slip condition for the contact line. Although it showed an improvement on the predicted interfacial curvature compared with the no-slip condition there was still not exact agreement with the results in Refs. [28] and [29].

In more recent publications, Gupta [45, 46] used a mesh partitioning technique to represent the interface between different polymer melt layers. In Refs. [45] and [46], a 3D tetrahedral mesh was used to discretize the full die geometry. The polymer–polymer interface was then captured by a separate surface mesh of linear triangular elements. The interface was allowed to pass through the core part of the die geometry, and new mesh shapes were created upon such intersection. Interfacial curvature was again produced numerically, but less than that predicted experimentally and without encapsulation. The lack of full, 3D encapsulation predicted numerically in the literature may be due to the wall conditions used and a lack of mesh refinement at the contact lines. Having movable meshes may lead to full encapsulation to be observed. Finite volume modeling, as used in this article, should not have the problematic contact line and pressure issues. This is because mass is conserved at every mesh cell including interfacial ones.

Interfacial curvature can have a detrimental effect on the final film properties [3]. To reduce this and produce a desired linear interface (see Fig. 1) either the different polymer melt viscosities should be similar or modifications to existing geometries can be made [8, 12, 13, 51, 52]. A method of viscosity matching of polymer melts is to change the temperature of one of the melts to get similar viscosities at the shear rates of interest, as shown in this study. It is also advisable to coextrude non-Newtonian polymers with similar viscosity–shear rate gradients so that viscosity matching is possible in all regions of the coextrusion hardware [53, 54].

Most previous publications on viscous effects in polymer coextrusion have investigated shear thinning polymer melts at a constant temperature. Since DTF's polyester melt viscosities are independent of shear rate but dependent on temperature, this approach is of limited relevance to this work. Karagiannis et al. [55] used a finite element code to demonstrate that nonisothermal effects in mono-component extrusion can lead to phenomena such as extrudate swell. When investigating polymer coextrusion, Sunwoo et al. [56] and Mallens and Waringa [17] implemented temperature effects into their finite element simulations. In Refs. [17] and [56] it was shown that changing the fluid temperature (and hence viscosity) can lead to an improved final structure and interfacial configuration based on viscosity matching. Temperature effects are relevant to this work and are analyzed both numerically and experimentally in this article.

Typically within DTF the polyester melt viscosity differences between resins are such that interfacial curvature rather than full encapsulation occurs. If the outer or secondary layer viscosity is sufficiently lower than the core or primary layer viscosity, the less viscous, thinner polymer will spread out to the film edges meaning that clear edges are not obtained. In this work, finite volume-based CFD is used to model an AB structured film produced using a DTF pilot scale injector block linked to a 410 mm wide die. The main advantages of the finite volume method compared with the finite element approach is that mass conservation is rigorously enforced and it offers greater efficiency when solving for complex geometries.

The temperature of each melt layer is varied, hence altering the viscosity ratio. One of the aims of this work, is to investigate the impact of temperature changes upon the secondary layer spreading and the final film structures. Both thermal and viscous effects are modeled, which leads to increased understanding since previous publications on polymer coextrusion have focused on viscosity as a function of shear rate and rarely temperature.

Another aim of this work, is to validate experimentally the CFD data. Die plug analysis, as demonstrated in Refs. [1, 11], and [38], allows for direct visualization of the flow behavior within the die and for comparison with the CFD predicted flow behavior. Chloroform washing of the outer soluble copolymer was applied to both cast and final, biaxially oriented film samples. This yielded individual A and B layer thickness data and subsequent comparisons with CFD and white light interferometry results. White light interferometry was applied to final film samples to also give individual layer thickness values. Neither chloroform washing nor white light interferometry have been used before to validate CFD analysis of multilayered films or polymer coextrusion. Interferometry was applied to multilayered sheets in Refs. [57] and [58] but this was to characterize the surface roughness rather than individual layer thickness values. A good agreement between numerical and experimental results is demonstrated in this article.

MATERIALS AND METHODS

Materials

The modeling was performed using the finite volume-based CFD software STAR-CCM+ Version 8.02.008 (CD-adapco) installed on a 32 GB Dell Precision T7500 Westmere workstation. The polymer properties and geometries modeled were representative of a pilot scale trial used to produce the AB structured film samples. Two different polymer melts were modeled for this purpose.

The film samples manufactured for experimental analysis were AB structures (Fig. 1a) of thickness between 20 and 25 μm. These samples were produced using an injector block linked to a 410 mm wide end fed die, which was replicated for

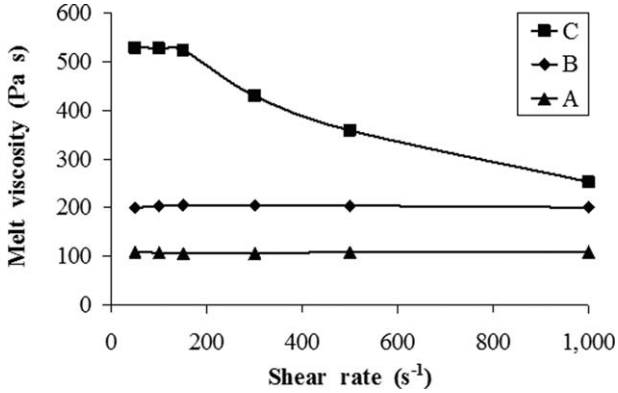

FIG. 2. Viscosity–shear rate curves for the primary PET (B), secondary co-PET (A), and red-PET (C) resins at a temperature of 280°C.

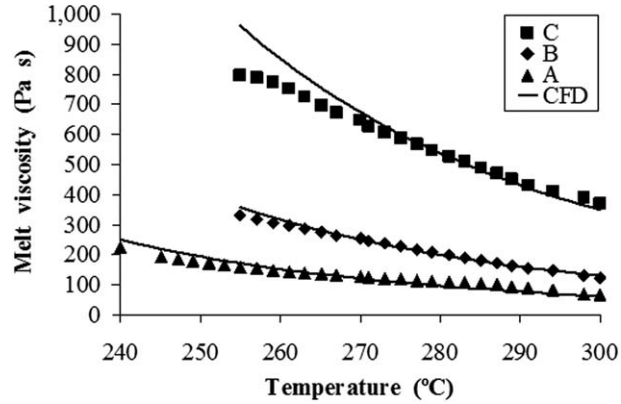

FIG. 4. Rheology of the primary PET (B), secondary co-PET (A), and red-PET (C) resins at an applied shear rate of 100 s^{-1}.

the CFD simulations. The primary B layer was a lightly filled PET polymer and the secondary A layer was a PET copolymer, making up around 25% of the overall final film thickness. For the final film sample obtained, the secondary A layer was made up of 93% co-PET and 7% red dyed, high viscosity PET (red-PET). This red-PET was added to the co-PET polymer for layer visualization purposes.

The three polymers used in this study are denoted PET (B), co-PET (A), and red-PET (C). Figure 2 shows how the melt viscosity of B, A, and C vary with shear rate ($\dot{\gamma} \leq 1000$ s^{-1}), measured using a rheometrics parallel plate rheometer. Newtonian behavior is exhibited by B and A up to 1000 s^{-1}. The high viscosity C resin shear thins at high shear rates but is Newtonian up to 150 s^{-1}, the maximum shear rate for the hardware and polymers used in this study. Therefore, a Newtonian assumption for PET is made throughout this article. The decrease in the viscosity of C observed at the higher shear rates is likely to be an artifact of the test; such high molecular weight PET is known to breakdown under these conditions.

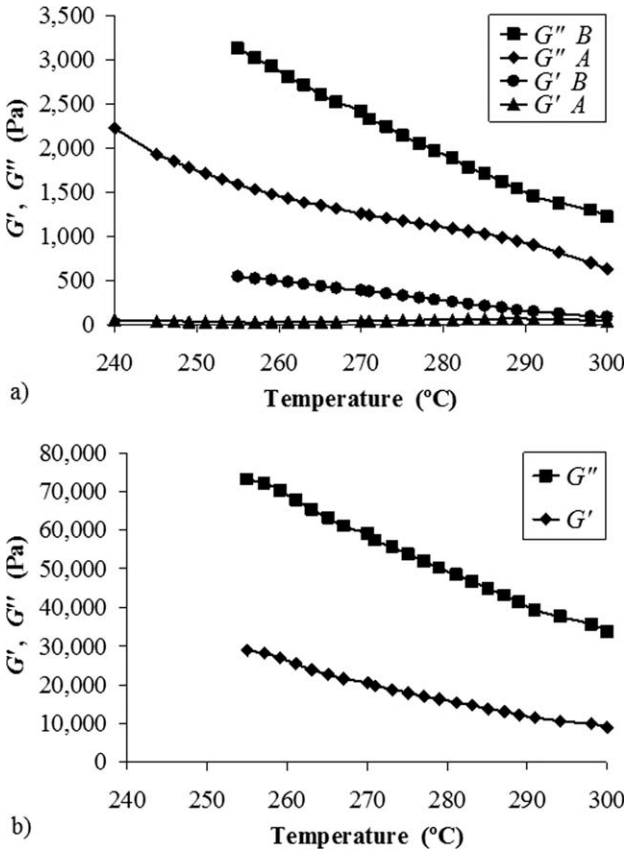

FIG. 3. The storage (G') and loss (G'') modulus at an applied shear rate of 100 s^{-1} for the three resins where: (a) shows the primary PET (B) and the secondary co-PET (A) polymers and (b) shows red-PET (C).

Figure 3 shows how the storage (G') and loss (G'') modulus of the three PET polymers vary with temperature at an applied shear rate of 100 s^{-1}, where Fig. 3a shows B and A and Fig. 3b displays C. This was also measured using a rheometrics parallel plate rheometer. Within the temperature range shown, $G'' > G'$ for all three resins. At the core processing temperature of 280°C, $\tan\delta$ is equal to 7.1, 21.9, and 3.1 for B, A, and C, respectively, where $\tan\delta = G''/G'$ [9]. This implies that viscous effects dominate over elastic ones for the three polymers used in this study and therefore elastic effects are not considered. Both the primary (N_1) and secondary (N_2) normal stress difference values are also used to ascertain the elasticity of a fluid [16, 59]. For the three PET polymers investigated in this study, Newtonian behavior is exhibited within the shear rates of interest (Fig. 2) and therefore $N_1 = N_2 = 0$ for B, A, and C [59]. This further justifies the inelastic assumption for PET used throughout this article.

Figure 4 shows the rheology of the PET (denoted B), co-PET (A), and red-PET (C) resins between 255 and 300°C for PET and red-PET and between 240 and 300°C for co-PET at a constant shear rate of 100 s^{-1}, where Newtonian behavior was assumed. The viscosity–temperature relationships (see Tables 2 and 3 in the next section) implemented in CFD to fit to these three datasets is also shown. At identical temperatures the primary PET polymer is more viscous than the co-PET resin, but the red-PET resin, as used in the final film sample, is the most viscous. It is common practice within DTF to process PET at

TABLE 1. The three film samples manufactured for experimental analysis.

Sample	Primary extruder	Secondary extruder	PET viscosity	co-PET viscosity
1	$T_{PET} = 280°C$	$T_{co\text{-}PET} = 280°C$	199 Pa s	109 Pa s
2	$T_{PET} = 290°C$	$T_{co\text{-}PET} = 265°C$	146 Pa s	135 Pa s
3	$T_{PET} = 290°C$	$T_{co\text{-}PET\ \&\ red\text{-}PET} = 265°C$	146 Pa s	≈175 Pa s

DOI 10.1002/pen

temperatures approaching 300°C. Within the total melt system residence time of 127 s for the polymers and hardware used in this study, thermal degradation is only observed at temperatures exceeding 300°C [60]. Differential scanning calorimetry was used to determine that the melting temperatures of PET and red-PET was 255°C and that of co-PET 220°C. Furthermore, the glass transition temperature of PET and red-PET was found to be 78°C and that of co-PET 76°C.

Three film samples at different processing conditions (temperatures) were manufactured. At the different extrusion temperatures, the viscosity difference between PET and co-PET is wider for Sample 1 compared with Sample 2. Therefore one would expect there to be more spreading of the thinner, less viscous co-PET layer to the film edges for Sample 1 [1, 8, 28, 45, 48]. The constant wall temperature of the injector block and die modeled was 280°C for all three samples.

Table 1 shows the processing conditions used for Samples 1–3. For Sample 1, both the PET and co-PET extrusion hardware were set at equal temperature $T = 280°C$, leading to a higher viscosity for the PET phase. For Sample 2, $T_{PET} = 290°C$ and $T_{co\text{-}PET} = 265°C$, which lead to improved viscosity matching as shown in Table 1. Sample 3 was identical to Sample 2 except for a small (7%) amount of red-PET placed within the co-PET polymer for layer visualization purposes. The secondary co-PET viscosity for Sample 3 was approximated using the co-PET and red-PET viscosity values at 265°C. Unlike the other two samples, the co-PET layer is more viscous than the PET layer for Sample 3. It is therefore expected that for Sample 3, the co-PET layer will not spread as much to the film edges and will be thicker in the middle of the film compared with Samples 1 and 2 [1, 4, 8, 17, 56].

Methods

Numerical Methods. CFD modeling of the two polymer melts flowing through DTF pilot scale coextrusion geometries was accomplished. Within the CFD domain, B was used to denote the primary PET melt flow and A the secondary co-PET melt. Full 3D CFD simulations were solved based on the assumption of incompressible, steady state and low Reynolds number flow with no body forces. The governing numerical equations for this nonisothermal, inelastic problem are shown in Refs. [11] and [56]:

$$\nabla . \underline{u}_k = 0, \tag{1}$$

$$\rho_k \underline{u}_k . \nabla \underline{u}_k = -\nabla p_k + \nabla . \underline{\underline{\tau}}_k, \tag{2}$$

$$(\rho c_p)_k \underline{u}_k . \nabla T_k = \kappa_k \nabla^2 T_k + \underline{\underline{\tau}}_k : \nabla \underline{u}_k, \tag{3}$$

which represent the mass continuity, momentum, and energy equations, respectively. In *Eqs. 1–3*, the subscript k is used to denote an individual melt phase within the coextrusion system; $k=1$ is B or PET and $k=2$ is A or co-PET. The symbols $\underline{u}$, ρ, p, $\underline{\underline{\tau}}$, c_p, and κ are the 3D velocity field, density, pressure, viscous stress tensor, specific heat capacity, and thermal conductivity, respectively, applying to individual melt phases. A no-slip condition (zero velocity at the geometry walls) was implemented throughout.

Two common dimensionless numbers used to quantify the viscous effects of polymer melts in coextrusion are the Reynolds number, *Re*, and the capillary number, *Ca*. *Re* is the ratio between inertial and viscous forces [23]:

$$Re = \frac{\rho u D}{\eta}, \tag{4}$$

and *Ca* is the ratio between viscous and surface (or interfacial) tension forces:

$$Ca = \frac{\eta u}{\sigma}, \tag{5}$$

where D is a length scale, η is the polymer melt viscosity, and σ is the surface (or interfacial) tension between the two fluids.

Approximations by Yue et al. [23] showed that for a typical polymer melt flow $Re \approx 10^{-4} \ll 1$, implying that inertial effects are negligible during coextrusion, and justifying the creeping flow assumption made in Ref. [23]. Again, for typical polymer melt flows (assuming $\sigma \approx 0.01$ N m^{-1}), Yue et al. [23] found $Ca \approx 10^3$, suggesting that the influence of interfacial tension between the two melt flows is negligible when they are in contact and thus it is not usually considered for numerical purposes [43, 61, 62]. For the polymers used in this study, $Ca \approx 2,000$. Thus, interfacial tension is not modeled in this article but inertial terms are included. Inertial terms are embedded within STAR-CCM+ and solving for these allows this work to not rely exclusively on the assumptions made in Ref. [23].

Discretized versions of *Eqs. 1–3* were solved for every mesh cell covering the CFD geometries at every iteration. The volume of fluid (VOF) method was used to numerically capture and track the interface between B and A. First published by Hirt and Nichols [63], the approach of the VOF method is to assign a volume fraction function, F, to every mesh cell, where $F=1$ corresponds to a cell full of B and $F=0$ implies a cell empty of B or full of A. Any cell such that $0 < F < 1$ is an interfacial cell, and $F=0.5$ is treated as the actual interface location.

Once the interface has been obtained at an initial time step, the interfacial evolution must be tracked at every subsequent iteration to interpret how this changes as the solution progresses. The evolution of F at time t is governed by the equation [63]:

$$\frac{DF}{Dt} \equiv \frac{\partial F}{\partial t} + \underline{u} . \nabla F = 0, \tag{6}$$

which alongside *Eqs. 1–3* provides a closed system of governing equations for the CFD simulations. Because of the unsteady nature of *Eq. 6*, implicit unsteady physics with a time step of 0.05 seconds per iteration was implemented into the model. The numerical methods used in this study are not as complex as those in (for example) Refs. [1, 23, 37, 43, 45, 46], and [50]. However, the simpler numerical approach is justified due to the Newtonian, inelastic nature of the PET melts modeled and readily enables the 3D complexity to be accounted for. The excellent agreement observed in this article between the numerical and experimental data gives further vindication of the numerical approach used.

To replicate the coextrusion hardware used to produce Samples 1–3, an injector block and a 410 mm wide end fed die were modeled. Figure 5 shows the meshed geometries created in STAR-CCM+, where Fig. 5a shows the injector block and Fig. 5b shows the end fed die. The flow direction in Fig. 5 is from right to left. The inlet duct diameter to the die is 23.75 mm, which then reduces to 22.5 mm for the remainder of the pipe as shown in Fig. 5b. The exit die gap increases when moving from

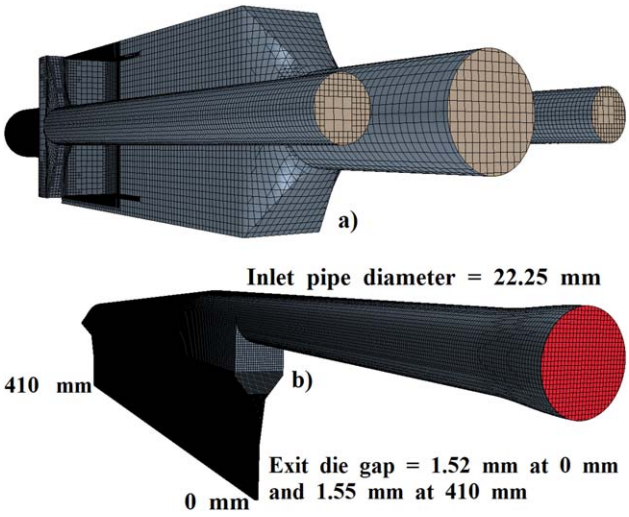

FIG. 5. The meshed CFD geometries used, where: (a) is the injector block and (b) is the 410 mm wide end fed die. The flow direction is from right to left. [Color figure can be viewed in the online issue, which is available at wileyonlinelibrary.com.]

0 to 410 mm edges to ensure a uniform exit flow across the die outlet width. The inlet pipe leading into the die is 196 mm long.

In the injector block geometry, there are two thinner secondary inlet channels and one primary inlet channel. To produce an AB structured film, the secondary A layer entered the block in the left side secondary channel. B entered the block in both the primary channel and right side secondary channel. A unified AB structure was produced at the injector block outlet. The injector block outlet solution was taken as an inlet condition into the end fed die. In the die, the unified melt structure is converted from a circular inlet into a thin rectangular outlet plot representative of the final film solution.

Around 1.5 million mesh cells were used to discretize the injector block with 14.5 million cells required for the end fed die. A trimmer mesh with hexahedral template cells was used for both geometries. Particularly fine mesh regions were selected when the melt flows were in contact with each other, with the aim of achieving a smooth, well defined interface between the different melt layers. A fine mesh (12 mesh cells across a gap of approximately 1.5 mm) was selected across the thin rectangular end fed die outlet due to the high aspect ratio in this study. For any CFD simulation, increasing the number of mesh cells leads to increased accuracy but there are limitations since a finer mesh will lead to longer convergence times and will require larger amounts of computer memory.

To represent the PET and co-PET melt layers in the coextrusion domain, fluid properties were assigned to both B and A in STAR-CCM+. Tables 2 and 3 shows the physical characteristics assigned to each melt where Table 2 shows the Sample 1 conditions and Table 3 shows Sample 3, assuming standard PET melt properties. The viscosity–temperature functions used are based on well established relationships within DTF and fit the rheology data as shown in Fig. 4. Melt viscosity is a function of molecular weight as well as temperature in these relationships.

TABLE 2. The modeled fluid properties for B and A for Sample 1.

	B (PET)	A (co-PET)
Temperature (T)	280°C	280°C
Density (ρ)	1250 kg m^{-3}	1250 kg m^{-3}
Viscosity (η), Pa s	$10^{\{(2{,}953/(T+273))-3.04\}}$	$10^{\{(2{,}953/(T+273))-3.36\}}$
Thermal conductivity (κ)	0.2 W $m^{-1}°C^{-1}$	0.2 W $m^{-1}°C^{-1}$
Mass flow rate ($\dot{m}$)	47.5 kg hr^{-1}	15.83 kg hr^{-1}
Final volume fraction	75%	25%

TABLE 3. The modeled fluid properties for B and A for Sample 3.

	B (PET)	A (co-PET & red-PET)
Temperature (T)	290°C	265°C
Density (ρ)	1250 kg m^{-3}	1250 kg m^{-3}
Viscosity (η), Pa s	$10^{\{(2{,}953/(T+273))-3.04\}}$	$10^{\{(2{,}953/(T+273))-3.25\}}$
Thermal conductivity (κ)	0.2 W $m^{-1}°C^{-1}$	0.2 W $m^{-1}°C^{-1}$
Mass flow rate ($\dot{m}$)	47.5 kg hr^{-1}	15.83 kg hr^{-1}
Final volume fraction	75%	25%

The secondary A or co-PET layer was modeled to make up 25% of the overall flow rate. The CFD simulations were set up to mimic the conditions of Samples 1–3 as described in Table 1. It was assumed that uniform flow from each extruder was delivered to the injector block inlet ports. Any interfacial smudging between A and B is a numerical artifact and is a function of the mesh cell size at a particular region.

Experimental Methods. Die plug analysis, chloroform washing of the co-PET layer and white light interferometry were used for experimental validation of CFD results. Die plug analysis was performed to analyze the flow within the 410 mm wide end fed die at the end of the pilot scale trial. Chloroform washing was applied to Samples 1–3 for both cast and biaxially oriented films to derive the secondary layer thickness profile across the whole film width. White light interferometry was conducted on final film samples to also give a secondary layer thickness profile. White light interferometry was not applied to cast film samples because the co-PET cast thickness is beyond the measurable limits for white light interferometry.

For die plug analysis, the end fed die was rapidly cooled at the end of the trial and a solid phase frozen polymer heel was produced. This polymer heel or die plug was carefully extracted from the end fed die. Since red dye was present in the secondary co-PET layer (see Sample 3 in Table 1), individual layer visualization was possible. The die plug was sectioned at different points across the die width. These sections were then scrutinized and compared directly with the CFD predicted layer configuration in the die when modeling Sample 3.

Chloroform washing was applied to both cast and final film samples, providing co-PET thickness profiles across the film width. The solvent chloroform (obtained from Sigma-Aldrich and used as received) was applied to the film surface in 2.5 mm spots across the film width, dissolving the thinner co-PET layer at each point. The film thickness was measured at each spot before and after chloroform application using a Sylvac D100S digital thickness gauge, calibrated using feeler gauges. The calibration performed internally implied a thickness gauge accuracy of 500 nm. This procedure was conducted three times across every film sample measured with averages taken, allowing for the total film and individual layer thicknesses to be obtained.

DOI 10.1002/pen

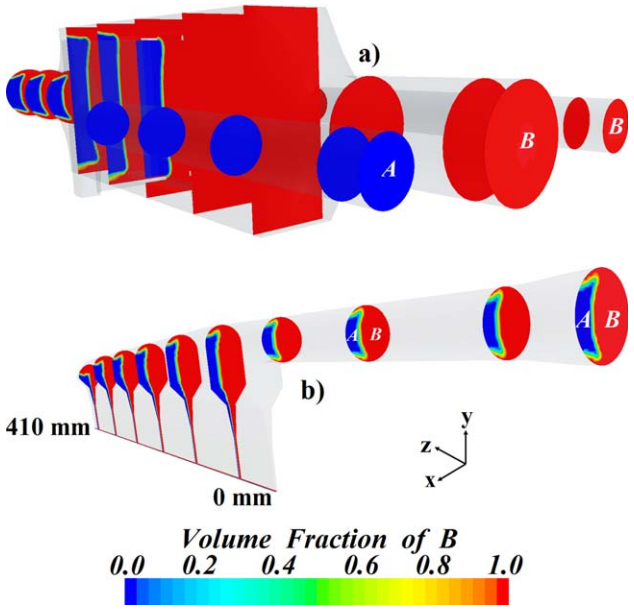

FIG. 6. The progressive volume fraction of B (shown in red) for Sample 1 through: (a) the injector block, where B enters through the two right inlet ports and (b) the end fed die, where B is on the right side of the unified structure. The flow direction is from right to left. The volume fraction of A is shown in blue and both B and A are labeled. [Color figure can be viewed in the online issue, which is available at wileyonlinelibrary.com.]

The thickness values derived for cast film analysis were converted, knowing the casting speed, and cast film density, to a volumetric flow rate per unit width across the die width, allowing for direct comparison with the CFD equivalent. For final film interpretation, the co-PET thickness values were compared with both the white light interferometry thickness values and the CFD co-PET flow values.

White light interferometry was used to obtain co-PET thicknesses for final film samples. A Veeco NT9800 interferometer, operating in vertical scanning interferometry (VSI) mode, was used. Small sections of the film samples were mounted onto a clear glass slide, ensuring as flat a field of view as possible. Once the film surface was in focus, a primary interferogram representative of the film surface was observed. The interferometric objective moved vertically downwards and a secondary interferogram, representative of the PET-co-PET interface was observed.

For the section of film measured, the Veeco software calculated the vertical distance between both interferograms and consequently an average co-PET thickness value. This is an average thickness value since the white light interferometry field of view is relatively wide containing a number of small pixels and the quoted thickness value is based on a point by point average difference. For the three film samples, white light interferometry was conducted three times in five different regions across the film width, with average co-PET thickness values generated. The total film thickness was measured at the points of white light interferometry application, generating the total and individual layer thickness profiles. The minimum vertical resolution of the Veeco NT9800 when operating in VSI is 3 nm.

When applying chloroform washing to final film samples, the secondary co-PET layer thickness was found to be too low compared with the equivalent white light interferometry and CFD results. A suggested reason for this is partial crystallization of the co-PET layer at the PET-co-PET interface when stretching and heating the film. Partial crystallization of the amorphous co-PET polymer would have resulted in a thin crystalline region that was insoluble in chloroform.

A method used to test the partial crystallization theory was time-of-flight secondary ion mass spectrometry (ToF-SIMS) surface analysis applied to Sample 1. The general operating principle of ToF-SIMS is as follows [64]: A primary positive ion source is directed toward a surface of interest. This causes charged secondary ions of varying size characteristic of the surface to be emitted. These secondary ions are detected by a time-of-flight detector and hence converted into a positive ion spectrum. The resulting spectrum can distinguish between different sized molecules because of their difference in mass and is then analyzed to determine the overall surface composition. ToF-SIMS, using a Bi_3^{2+} ion source, was applied to three different Sample 1 surfaces: The untreated PET and co-PET sides and the co-PET side after applying chloroform (the PET–co-PET interface). The spectrum for the chloroform treated co-PET side was then compared with the PET and co-PET spectra to determine whether any co-PET was present at the interface.

RESULTS AND DISCUSSION

Numerical Simulations

Figure 6 shows the CFD predicted volume fraction of B through both the injector block (Fig. 6a) and the end fed die (Fig. 6b) for Sample 1 (Table 1). In Fig. 6, B is in red, A in blue, and the flow direction is from right to left.

Polymer B is shown to enter the injector block through the main primary inlet channel and the right secondary inlet channel, with A entering through the left secondary inlet. The melt layers then come together within the block to form a unified AB structure with A making up 25% of the overall composition. There is a smooth, well defined interface throughout between the two melt flows within the injector block and end fed die, implying a sufficiently fine mesh within the domain once the fluids are in contact.

The volume fraction and other results at the injector block outlet were taken as initial conditions into the end fed die. In the die, the circular melt structure is converted into a uniformly thin rectangular melt curtain at the outlet upon entering the main die body from the inlet pipe. The direction of flow within the die changes from horizontal (z) to both horizontal and vertical ($-y$) when moving from the pipe into the main part of the die. A volume fraction plot of B at the die outlet is what defines the CFD predicted final film structure. This is shown for Sample 1 in three 45 mm sections at the die outlet in Fig. 7, where Fig. 7a shows the section from the 0 mm edge to 45 mm, Fig. 7b shows the middle, from 180 to 225 mm, and Fig. 7c displays from 365 mm to the far edge at 410 mm.

Figure 7a and c show that CFD does not predict the formation of clear edges at either edge of the Sample 1 final film structure with the blue A layer present at each edge. This is despite clear edges being attainable for actual multilayered films produced using the injector block and end fed die system. The lack of numerical clear edges is attributed to the high degree of spreading of the lower viscosity A to the film edges (see Table

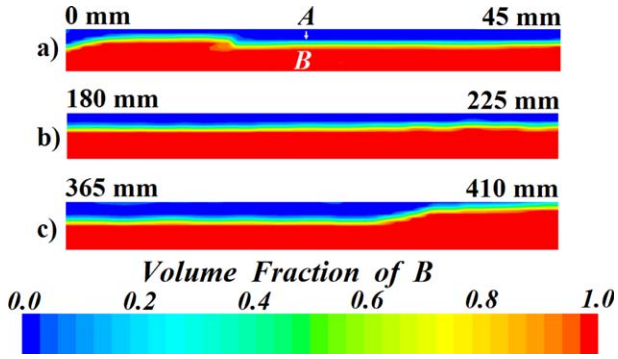

FIG. 7. The volume fraction of B (shown in red, the bottom layer) at the die outlet for Sample 1 showing: (a) the 0 mm edge, (b) the middle, and (c) the 410 mm edge. The volume fraction of A is shown in blue and is the top layer. [Color figure can be viewed in the online issue, which is available at wileyonlinelibrary.com.]

1, Sample 1). Also, numerical diffusion errors exacerbate this, particularly at the 0 mm edge where the flow goes through a sharp 90° transition on entering the die body [65]. In the context of this work, the numerical diffusion is not significant and the CFD results are shown experimentally to accurately represent the die plug and both cast and final film solutions in all but the extreme edges.

There is more A present at the 0 mm edge compared with the 410 mm edge. This greater bias of spreading towards the 0 mm edge is observed in reality but is exaggerated numerically. As mentioned in the previous paragraph, the flow is not properly resolved at the sharp transition point from the horizontal to vertical flow direction in the end fed die. The 0 mm edge profile at the outlet may have improved with the input of a finer mesh at this region but this would have increased the total convergence time. The number of mesh cells possible is a limitation of this study, however apart from the excess amount of A at the 0 mm edge the final film structure in Fig. 7 is similar to what was obtained experimentally.

The volumetric flow rate per unit width across the whole die outlet width was derived for the total and co-PET flows, with flow curves plotted in each case. These flow curves correspond to the CFD predicted total film and co-PET thickness profiles across the die width. To derive the total flow curves, lines were created in the CFD domain across the exit die gap from 0 to 410 mm in increments of 1 mm. The outlet velocity magnitude was then integrated across each line using the CFD software, yielding the total volumetric flow rate per unit width (measured in $m^2\ s^{-1}$) for every line. For the co-PET flow curves, the same procedure was performed on lines spanning the co-PET outlet location from the top outlet wall (see Fig. 7) to the $F=0.5$ interfacial location, where F is the volume fraction function.

These flow curves are shown graphically in Fig. 8 for Samples 1–3, where Fig. 8a shows the comparative total flows and Fig. 8b shows the secondary co-PET flows. Comparing the total flow curves, a similar profile is observed in each case, with the flow falling to zero at each end of the film as expected due to the no-slip condition. A uniformly thin final film is obtained for the three samples, which is desirable from a commercial perspective. The CFD obtained edges were thickest for Sample 1, particularly at the 410 mm edge. This is believed to be due to a greater spreading of the co-PET layer to the extreme edges in Sample 1. For Samples 1 and 2, co-PET is less viscous than PET. Since the viscosity difference is wider in Sample 1 (Table 1), the co-PET layer spreads more. For Sample 3, co-PET is more viscous than PET, with co-PET therefore not spreading as much as in Sample 1.

Analysis of the co-PET CFD flow curves in Fig. 8b again shows that there is more of the less viscous co-PET at the extreme edges for Sample 1 than Samples 2 and 3. This is again due to the greater viscosity difference in Sample 1. Sample 3 has the most co-PET present in the middle of the film, caused by the co-PET layer remaining confined to the center since it is more viscous than PET. The flow differences in Fig. 8 are noticeable but the film structures have not changed significantly despite temperature and hence melt viscosity differences. This suggests that from a CFD perspective, the rheology difference for Sample 1 does not have a negative impact on the final film thickness and is within the limits of DTF pilot scale facilities. Improved control and measurement of the melt temperature of both streams may increase understanding of the solutions.

There is significantly more noise in the co-PET flow data than the total flow data. This is because the flow calculations to obtain Fig. 8b are based on numerical approximations of the exact interfacial location. At the die outlet, the $F=0.5$ interfacial contour changes position within a mesh cell when moving from 0 to 410 mm across the die. The outlet mesh is coarse with respect to the $F=0.5$ contour so the exact $F=0.5$ interfacial location cannot be determined. To amend for this, STAR-CCM+ uses a smoothing function (linear in the flow direction) to estimate the $F=0.5$ position in every interfacial mesh cell.

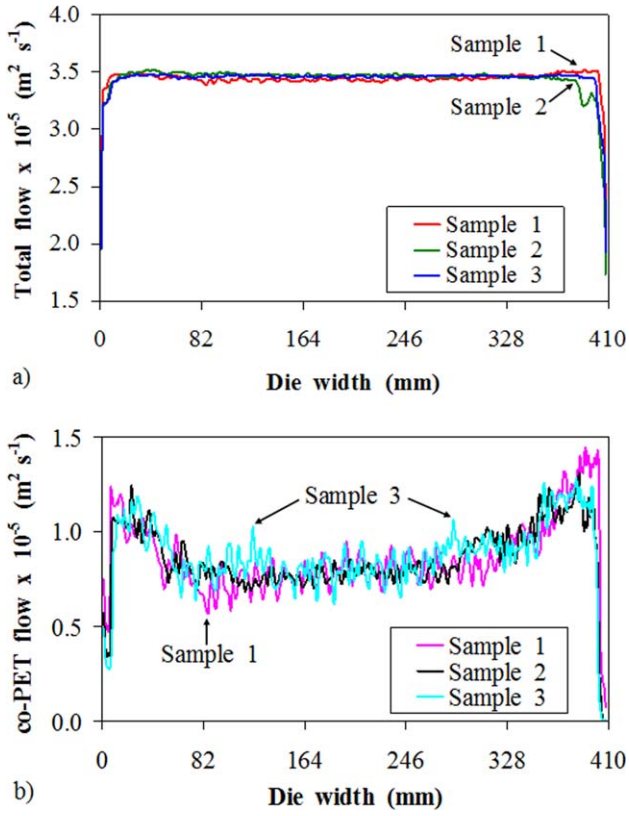

FIG. 8. The CFD predicted die outlet flow plots for Samples 1–3, where (a) is the total flow and (b) is the secondary co-PET flow. [Color figure can be viewed in the online issue, which is available at wileyonlinelibrary.com.]

DOI 10.1002/pen

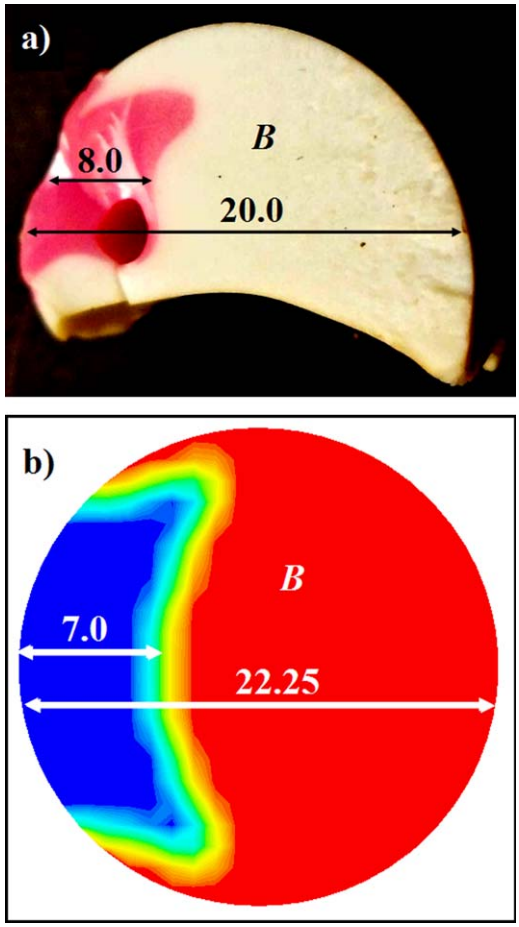

FIG. 9. The flow configurations 125 mm into the inlet pipe for Sample 3 where (a) shows the die plug structure and (b) shows the CFD structure. The primary polymer B is labeled in each figure. All dimensions shown are in millimeters. [Color figure can be viewed in the online issue, which is available at wileyonlinelibrary.com.]

This leads to noisy data which would be ameliorated with a finer mesh or smoothing the data in the axial direction along the die body, again showing numerical limitations of this work. For the purpose of this work, the overall co-PET flow trend rather than the noise is important. As shown in the next section, there is an excellent agreement between CFD and chloroform washing of cast film samples based on the co-PET flow trend.

Experimental Findings

The experimental results are split into two sections: Overall flow validation and secondary layer thickness validation. Die plug analysis and thickness measurements via chloroform washing of cast film samples are shown in the overall flow validation section. The secondary layer thickness validation section shows both white light interferometry and chloroform washing applied to final, biaxially oriented film samples with the secondary layer thickness calculated. Comparison with the numerical results are made throughout.

Overall Flow Validation

At the Sample 3 conditions, a die plug was obtained showing the individual layer configuration between the PET and co-PET layers through the die. The die plug was obtained after rapid cooling of the die and was sectioned in ten points across the inlet pipe and die width. A small amount of red-PET present in the co-PET layer allowed for determination of both layers. The die plug layer structures were then compared with the CFD predicted Sample 3 configurations at the equivalent sections in the pipe or die.

At 125 mm into the inlet pipe, Fig. 9 shows the PET-co-PET individual layer configuration, where Fig. 9a shows the die plug structure and Fig. 9b shows the CFD predicted structure. In Fig. 9a, PET is in white and co-PET in pink and in Fig. 9b, PET is in red with co-PET in blue. In general there is good agreement between the two plots, with the overall flow shape and degree of interfacial curvature observed experimentally validating the numerical result. A section of the die plug is missing at the bottom of Fig. 9a and this shows a break in the die plug upon extraction from the end fed die geometry. This highlights the difficulties associated with removal of the die plug from such a narrow end fed die.

Further differences between Fig. 9a and b are based on both the diameter of the whole structure and the co-PET layer width. The diameter of the experimentally obtained die plug is 20.0 mm, compared with 22.25 mm for CFD. This difference is due to the density increase in PET during the transition from a melt to a solid structure so the die plug shrunk when cooled. Furthermore, the co-PET layer is wider in the die plug. This is because of the lower melting point of co-PET compared with PET and the molten co-PET spreading further toward the center of the pipe when cooled. Despite these differences there is generally a good agreement between the die plug and CFD individual layer results.

Repeating the comparisons 335 mm into the die (see Fig. 10) again shows that the die plug (Fig. 10a) has validated the CFD flow profile (Fig. 10b). There is an excellent match between the co-PET structures in each case. The main differences between Fig. 10a and b are the overall die plug height and secondary co-PET layer width. These differences are attributed to the breaking of the die plug upon removal and different polymer layer melting temperature differences respectively. Similar agreement was observed for the eight other die plug sections in either the inlet pipe or the die body (not shown). An excellent agreement

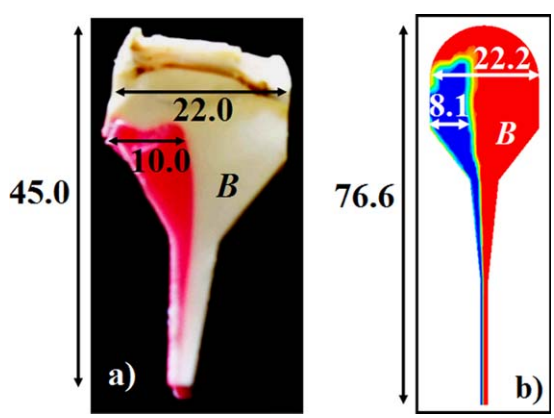

FIG. 10. The flow configurations 335 mm into the die body for Sample 3 where (a) shows the die plug structure and (b) shows the CFD structure. The primary polymer B is labeled in each figure. All dimensions shown are in millimeters. [Color figure can be viewed in the online issue, which is available at wileyonlinelibrary.com.]

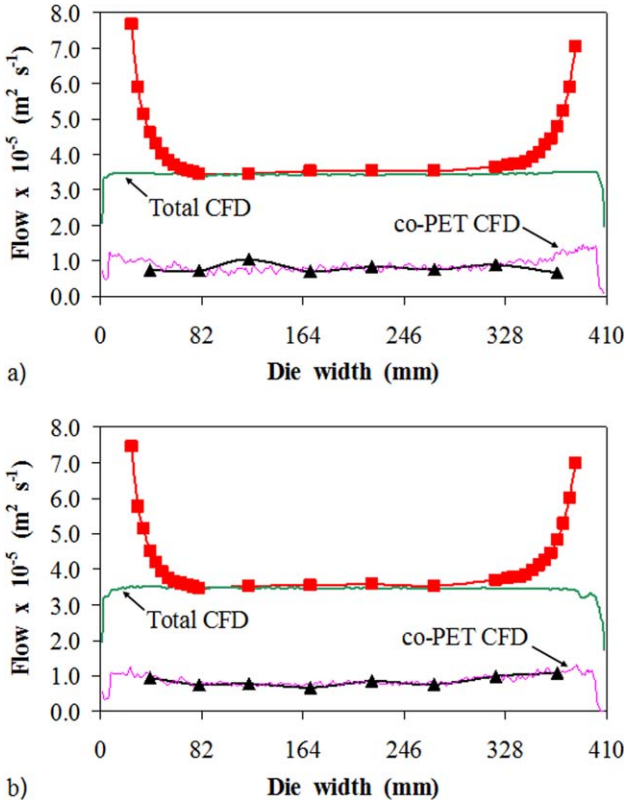

FIG. 11. The total and co-PET flow curves across the die outlet width for both chloroform washing and CFD where (a) shows Sample 1 and (b) shows Sample 2. For the curves in both figures, the total chloroform washing flow is in red (■), the total CFD flow is in green, the co-PET chloroform washing flow is in black (▲), and the co-PET CFD flow is in pink. [Color figure can be viewed in the online issue, which is available at wileyonlinelibrary.com.]

between die plug structures and numerically predicted phase distributions is also shown in Refs. [1, 22, 37], and [66].

To complement the Sample 3 die plug analysis, chloroform washing was performed on Samples 1 and 2 as cast (unstretched) film. Chloroform was applied across the film widths, producing thickness profiles for the total film and the secondary co-PET layer. These thickness values were then converted to a volumetric flow rate per unit width across the film width using both the casting drum speed and the cast film density (corrected for the ambient to PET melt temperature ratio). These flow results allow for direct comparison with the CFD flow curves in Fig. 8, as shown in Fig. 11, where Sample 1 and Sample 2 results are presented in Fig. 11a and b, respectively. Each figure shows the chloroform washing and CFD obtained total and co-PET flow curves.

Observation of the total flow curves in Fig. 11 shows a large increase at the edges for chloroform washing compared with CFD. This is due to a phenomenon known as neck-in of the cast film [67, 68]. When a melt curtain exits a polymer die, it is stretched by a factor of around five by the casting drum. Since its edges are unsupported during this stretching, the edges are not stretched as much, and the melt curtain and hence cast film width narrows. The phenomenon of neck-in was not modeled with CFD, with the solution obtained for the die outlet being taken as representative of the final film.

The Sample 1 and Sample 2 cast film width is 370 mm, implying a neck-in of 20 mm from each edge based on a 410 mm wide end fed die. The measurement range of the total chloroform washing flow data in Fig. 11 is from 5 to 365 mm across the 370 mm cast film width. This is plotted from 25 to 385 mm across the 410 mm die width to correct for the 20 mm neck-in and allow for a direct comparison with the CFD flow data. The co-PET chloroform washing flow curves in Fig. 11 are based on thickness measurements between 20 and 350 mm across the cast film width. These are plotted from 40 to 370 mm across the die width to again account for neck-in.

Integrating the Sample 1 and Sample 2 chloroform washing and CFD total flow curves and subsequently multiplying this by either the cast or melt density gives a value of 0.018 kg s^{-1} to three decimal places for all curves. The percentage difference between the CFD and chloroform washing mass balance values was 3.16% for Sample 1 and 3.52% for Sample 2. This confirms a conservation of mass within a 5% error despite neck-in not being modeled with CFD.

There is generally a good agreement between the chloroform washing and CFD flow results for Sample 1 (Fig. 11a). The main part of the total chloroform washing flow curve matches its CFD equivalent well. There is also a good correlation between the two co-PET flow curves except for two ambiguous chloroform washing results at 100 and 350 mm across the cast film width (plotted at 120 and 370 mm to correct for the 20 mm neck-in). These outliers are believed to be due to human error when performing chloroform washing, with either the primary PET layer being partially dissolved or excess co-PET remaining on the film surface at 100 and 350 mm, respectively.

An even better agreement between CFD and chloroform washing is found for Sample 2 (Fig. 11b), with an excellent match between experimental and numerical flow curves. Chloroform washing of cast film samples has validated the CFD outlet flow predictions at the range where data was obtained. These results alongside the die plug analysis confirm the successful validation of CFD flow results.

Secondary Layer Thickness Validation

For final, biaxially oriented film Samples 1–3, both white light interferometry and chloroform washing were applied. This was to calculate the secondary co-PET thickness profile across the final film width of 800 mm. Comparisons between white light interferometry, chloroform washing, and CFD for co-PET thickness measurements are shown in this section.

Figure 12 shows an example screenshot taken from white light interferometry applied to the middle of Sample 2. For all white light interferometry measurements, a primary topography plot showing the film surface (see Fig. 12a) was obtained. The interferometric objective then moved vertically downwards, generating a secondary interfacial topography plot (see Fig. 12b). The *z*-scale color bars to the right of Fig. 12a and b show the height information in micrometers for each plot. The software then calculated the vertical distance between the two topography plots at each point, and hence generated a co-PET layer thickness plot (see Fig. 12c). The size of the three images in Fig. 12 is 2.5 × 1.9 mm, or 640 × 480 pixels. The co-PET layer thickness plot in Fig. 12c is therefore calculated from 307,200 measurement points.

DOI 10.1002/pen

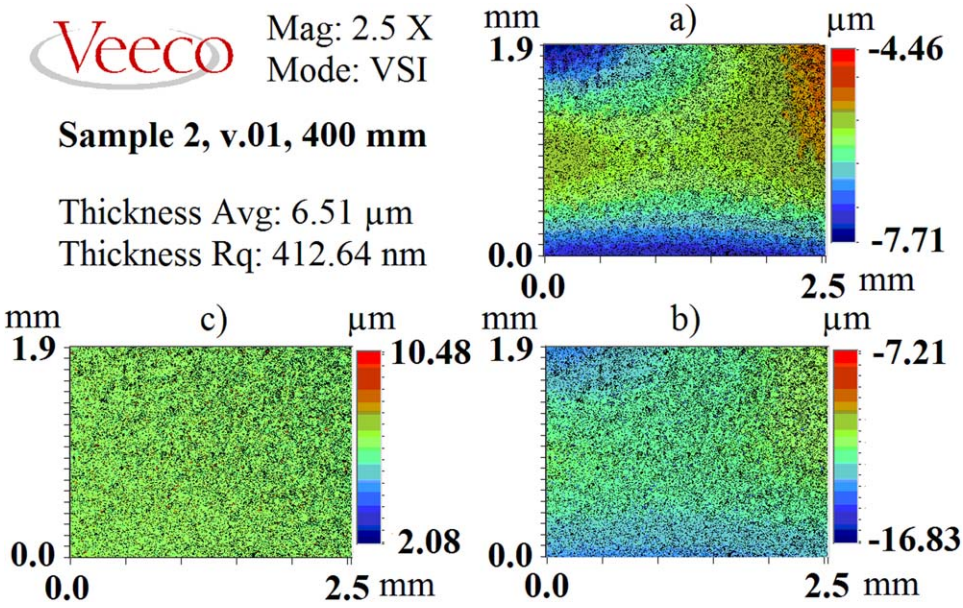

FIG. 12. A white light interferometry screenshot showing analysis of Sample 2 400 mm into the film, where (a) shows the primary surface topography plot, (b) shows the secondary interfacial topography plot, and (c) shows the co-PET thickness topography plot. The average co-PET thickness is calculated as 6.51 µm. [Color figure can be viewed in the online issue, which is available at wileyonlinelibrary.com.]

The average co-PET layer thickness is calculated from the plot in Fig. 12c. For the calculation in Fig. 12, the average co-PET thickness is found to be 6.51 µm, but the thickness range is from 2.08 to 10.48 µm. White light interferometry is a high resolution point by point measurement technique and can detect surface roughness accurately. The large thickness range in Fig. 12 implies either a film surface or interfacial roughness that one must be aware of when further analyzing white light interferometry results. For Samples 1–3, white light interferometry as shown in Fig. 12 was performed three times at five locations across the film width with average co-PET thickness values taken.

Figure 13 shows the white light interferometry calculated average total film and individual layer thickness profiles, where Fig. 13a and b show results for Samples 1 and 2, respectively. Measurements were taken at locations 50, 200, 400, 600, and 750 mm across the film width. The data points in Fig. 13 are based on an average of three measurements. At each of the five measurement locations, there was little difference between the three thickness values obtained. This shows sample consistency for white light interferometry and a low sample variance or a high repeatability with white light interferometry between the three measurements at each point across the film.

There is however a relatively high method variance associated with these white light interferometry results. For any co-PET thickness measurement, the Veeco software quoted the value subject to a roughness value or measurement error R_q (see Fig. 12) for the white light interferometry measurement technique. The average co-PET thickness for Samples 1 and 2 is 6.4 µm, using the five data points in Fig. 13. The values taken across the film width to obtain these averages are typically subject to an R_q of 400–600 nm, or an error of ±6–9%. This method variance is caused by smooth surface undulations in the

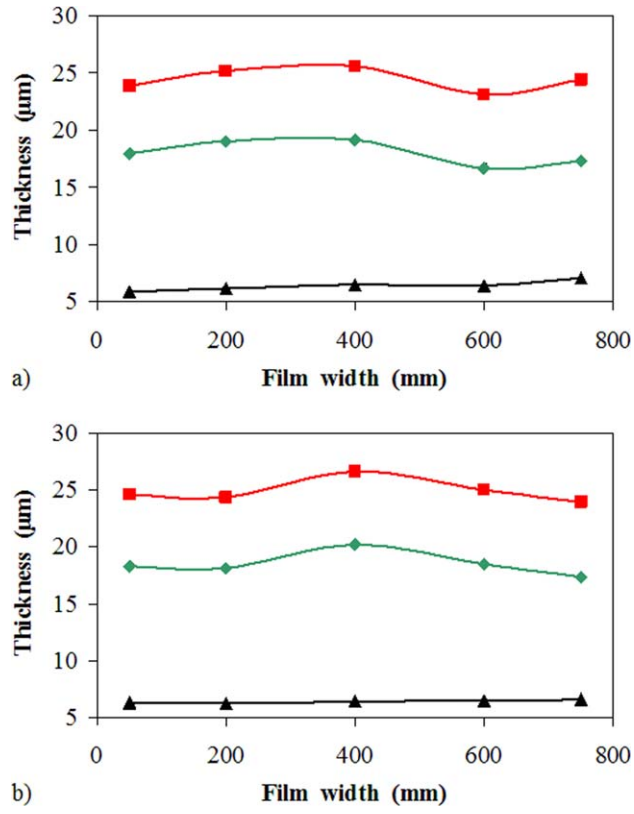

FIG. 13. The white light interferometry measured average total film, PET and co-PET thickness for (a) Sample 1 and (b) Sample 2. For the curves in both figures, the total film thickness is shown in red (■), the primary PET thickness is in green (◆), and the secondary co-PET thickness is in black (▲). The error bars are within the range of the symbol height. [Color figure can be viewed in the online issue, which is available at wileyonlinelibrary.com.]

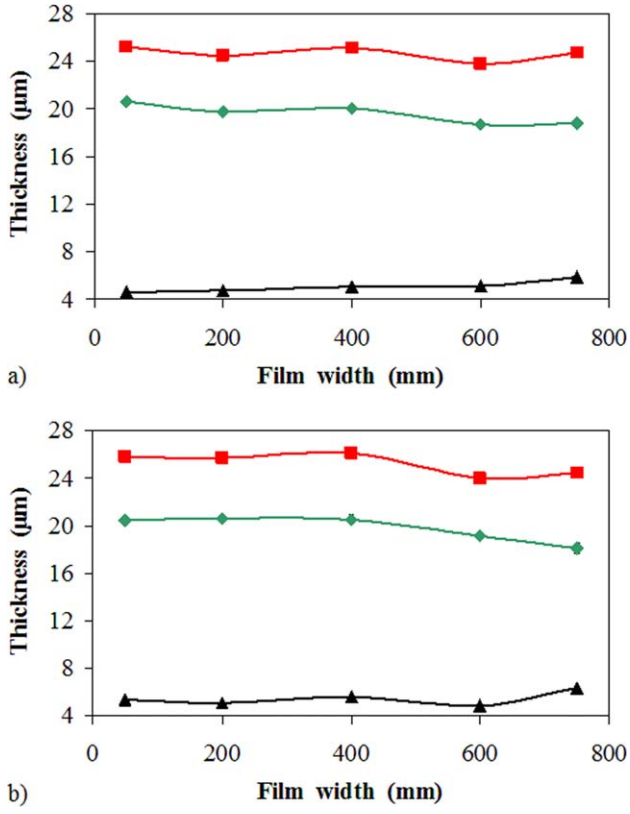

FIG. 14. The chloroform washing measured average total film, PET, and co-PET thickness for (a) Sample 1 and (b) Sample 2. For the curves in both figures, the total film thickness is shown in red (■), the primary PET thickness is in green (◆), and the secondary co-PET thickness is in black (▲). The error bars are within the range of the symbol height. [Color figure can be viewed in the online issue, which is available at wileyonlinelibrary.com.]

co-PET surface layer, as films containing this polymer require a degree of surface roughness. Another factor causing a high method variance is the low signal to noise ratio when measuring the interfacial location through the film surface.

From Fig. 13, the total Sample 1 and Sample 2 film thickness is highest in the middle of each film. The maximum co-PET thickness is at the far 750 mm edge, again for both samples. At this edge, a thicker co-PET layer is found for Sample 1 (7.1 μm) compared with Sample 2 (6.6 μm). This is as expected given the lower viscosity of co-PET compared with PET in Sample 1 [1, 4, 8, 10, 48]. At the 50 mm edge measurement, the quantity of co-PET is found to be greater in Sample 2 than Sample 1. This is opposite to what was expected but is within the method variance range.

The equivalent chloroform washing results for the average total film and individual layer thickness profiles are shown in Fig. 14, where Fig. 14a shows Sample 1 and Fig. 14b shows Sample 2 results. The data points in Fig. 14 are again based on an average of three measurements at five locations across the film width. Compared with the white light interferometry results, there was a far greater difference between the three thickness measurements taken at each location for chloroform washing results (see the error bars in Fig. 15). This shows poor repeatability of the chloroform washing results or a high sample variance. Chloroform washing is not as rigorous as white light interferometry, and this alongside measurement error of the digital thickness gauge is believed to cause the sample variance. The average co-PET thickness when using chloroform washing is 5.1 μm for Sample 1 and 5.5 μm for Sample 2.

Figure 15 shows a combination of Figs. 13 and 14, where the average co-PET thickness profiles of Samples 1 and 2 are plotted using both white light interferometry and chloroform washing. At this smaller *y*-axis range, the high chloroform washing sample variance is detectable via the significantly higher error bars compared with white light interferometry. The general trend in the four thickness profiles shows an increase in the co-PET thickness when moving from 50 to 750 mm. This may be due to an injector block secondary layer inlet port geometry or temperature differences slightly favoring flow toward the far edge of the film when manufacturing the three film samples. At the 750 mm edge, the amount of co-PET is higher for Sample 1 than Sample 2 with white light interferometry as expected. The reverse is found for the chloroform washing results but these thickness differences are within the range of the error bars or sample variance.

For the five data points in Fig. 15, there is a thickness difference between both measurement techniques, with white light interferometry consistently measuring a 1 μm thicker co-PET layer for identical film samples. The inconsistency of the two methods is attributed to both white light interferometry method variance and chloroform washing sample variance. Despite differences between the measurement techniques, the Sample 1 and Sample 2 results are fairly consistent. This suggests that the temperature and hence polymer melt viscosity differences were not wide enough to significantly change the co-PET spreading. This was also found numerically and future work will need to repeat the analysis in this article on more rheologically different polymer melts.

For the three biaxially oriented final film samples, Table 4 shows the average co-PET layer thickness as a percentage of the total film thickness for white light interferometry, chloroform washing, and CFD. The percentage thickness values in Table 4 are based on an average of the thickness data obtained at the five measurement locations across the film width for white light

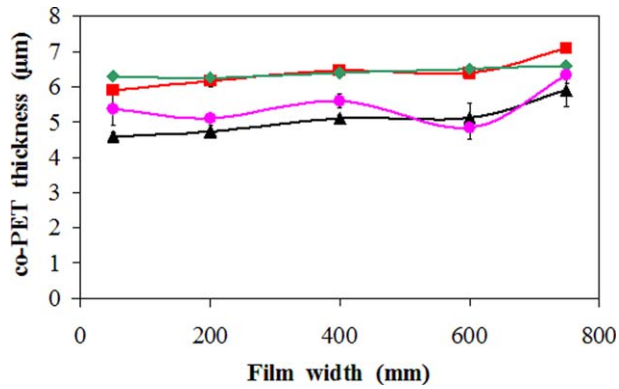

FIG. 15. The average Sample 1 and Sample 2 co-PET thickness profiles using both white light interferometry and chloroform washing. In this study, white light interferometry analysis of Sample 1 is in red (■), white light interferometry analysis of Sample 2 is in green (◆), chloroform washing analysis of Sample 1 is in black (▲), and chloroform washing analysis of Sample 2 is in pink (●). The white light interferometry error bars are within the range of the symbol height. [Color figure can be viewed in the online issue, which is available at wileyonlinelibrary.com.]

DOI 10.1002/pen

TABLE 4. The percentage co-PET thickness of the total film thickness using both experimental and numerical methods for all three film samples.

Sample	White light interferometry (%)	Chloroform washing (%)	CFD (%)
1	26.2	20.6	24.9
2	25.8	21.6	24.6
3	27.1	22.6	26.6

interferometry and chloroform washing. The CFD thickness values are based on an average of the co-PET flow calculations as a percentage of the total flow calculations at the equivalent five measurement locations across the die width.

White light interferometry shows a significantly better agreement with CFD than chloroform washing. The white light interferometry results are slightly higher than the CFD equivalent but these thickness differences are within the measurement error or method variance range for this technique. For validating CFD results, white light interferometry is shown to be more accurate than chloroform washing. A reason for this is that unlike chloroform washing, white light interferometry is non-intrusive to the film surface and the secondary co-PET layer is not disturbed or damaged. White light interferometry is also better than chloroform washing at capturing fine surface or interfacial detail. White light interferometry is the more accurate and robust measurement technique and is less susceptible than chloroform washing to human or experimental error.

From Table 4, the chloroform washing data for final film samples is too low compared with CFD and does not fully validate the numerical results. Comparing Table 4 with Fig. 11 implies that the chloroform washing data is inconsistent between cast and equivalent final film samples of the same film. It appears that more co-PET was retained on the final film than the cast film upon chloroform application.

A suggested reason for this is partial crystallization of the co-PET layer at the PET–co-PET interface when stretching and heating the film. A white light based reflectometry technique (not shown) also yielded too low co-PET thickness values, further justifying the partial crystallization theory. Partial crystallization of the amorphous co-PET polymer would have resulted in a thin crystalline region that was insoluble in chloroform. This crystalline region therefore remains on the film at the PET-co-PET interface upon chloroform application, and the co-PET thickness is measured to be lower than its actual value for final film samples.

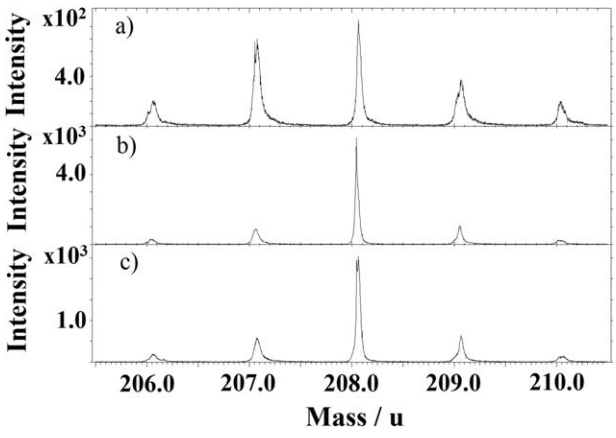

FIG. 16. ToF-SIMS positive ion spectra showing: (a) unwashed PET, (b) unwashed co-PET, and (c) chloroform washed co-PET surfaces for Sample 1.

A second method used to test the partial crystallization theory was ToF-SIMS surface analysis applied to Sample 1. ToF-SIMS, using a Bi_3^{2+} ion source, was applied to three different surfaces: the untreated PET and co-PET sides and the co-PET side after applying chloroform (the PET–co-PET interface). If the co-PET had been fully dissolved by the chloroform, one would expect the washed co-PET spectrum to exactly match the unwashed PET one. However, the three spectra observed (see Fig. 16) shows that the washed co-PET spectrum (Fig. 16c) instead matches the unwashed co-PET result (Fig. 16b). This confirms that there is still some co-PET present on the film after chloroform application, hence the low chloroform washing thickness results. The suggested, logical reason for this is partial crystallization of the co-PET layer at the interface.

The thickest co-PET layer is found both experimentally and numerically in Sample 3. This suggests that the addition of the red-PET increased the co-PET rheology, with less spreading to the edges in Sample 3 compared with Samples 1 and 2. This reduced co-PET spreading for Sample 3 is what one would expect given the data shown in Fig. 4 and Table 1 [1, 4, 8, 17, 28, 29, 48, 56].

CONCLUSIONS

Die plug analysis, chloroform washing, and white light interferometry were used to validate CFD modeling of polyester coextrusion. There was a good agreement between die plug structures and CFD results, with a good correlation based on the degree of encapsulation and the overall flow configuration. Both cast and final, biaxially oriented multilayered film samples were manufactured for experimental purposes.

For cast film analysis, excellent agreement was found between chloroform washing and CFD when comparing flow curves. When investigating final films, the white light interferometry obtained secondary co-PET thickness values validated CFD within the bounds of experimental error. However, the chloroform washing results for final films were found to be too low compared with both CFD and cast film results. This is attributed to partial crystallization of the co-PET layer upon orienting the cast film. There was generally a good agreement between numerical and experimental results and CFD modeling of polyester coextrusion was validated in this article at the data points analyzed.

The temperature and hence viscosity differences between the primary PET and secondary co-PET melt layers did not cause significant changes in the final film structures. It is envisaged that more rheologically different polymer melt flows would cause greater changes in the final film systems. Similarly, changing the amount of red-PET present in the co-PET layer would alter the layer composition.

ACKNOWLEDGMENTS

The authors gratefully acknowledge John Francis (DuPont Teijin Films) for providing chloroform washing training, Karl Rakos and David Bell (DuPont Teijin Films) for providing white light interferometry training, David Stocks (Intertek) for the rheological characterization of the polymers involved and Ian Fletcher (Intertek) for ToF-SIMS surface analysis.

REFERENCES

1. J. Dooley, *Viscoelastic Flow Effects in Multilayer Polymer Coextrusion*. PhD Thesis, Technische Universiteit Eindhoven (2002).
2. J. Dooley and K. Hughes, *TAPPI PLACE Conference*, 85 (1995).
3. M.T. Martyn, R. Spares, P.D. Coates, and M. Zatloukal, *J. Non-Newton. Fluid Mech.*, **156**, 150 (2009).
4. C. Rauwendaal, *Polymer Extrusion*, 4th ed., Hanser Gardner Publications, Munich (2001).
5. D.W. Brooks and G.A. Giles, *PET Packaging Technology*, Sheffield Academic Press, London (2002).
6. C.D. Han, *Rheology and Processing of Polymeric Materials, Vol. 2, Polymer Processing*, Oxford University Press (2007).
7. C.D. Han and R. Shetty, *Polym. Eng. Sci.*, **16**, 697 (1976).
8. D. Djordjevic, *Coextrusion*, Vol. 6, Rapra Review Reports, UK, 1 (1992).
9. R.S. Lenk, *Polymer Rheology*, Applied Science Publishers Ltd., London 31 (1978).
10. G. Oliver, *TAPPI* (2010), http://www.tappi.org/content/events/10EXTRU/papers/3.3.pdf.
11. J. Dooley, H. Kim, P.C. Lee, and R. Wrisley, *ANTEC*, **59**, 994 (2013).
12. E. Mitsoulis, *Adv. Polym. Technol.*, **8**, 225 (1988).
13. X.-L. Luo and E. Mitsoulis, *Adv. Polym. Technol.*, **10**, 47 (1990).
14. K. Lamnawar, H. Zhang, and A. Maazouz, "Coextrusion of Multilayer Structures, Interfacial Phenomena," in *Encyclopedia of Polymer Science and Technology*, John Wiley & Sons 1 (2013).
15. H. Zhang, K. Lamnawar, and A. Maazouz, *Polym. Eng. Sci.* (2014). DOI: 10.1002/pen.23945.
16. K. Lamnawar and A. Maazouz, *Polym. Eng. Sci.*, **49**, 727 (2009).
17. R.M.M. Mallens and C.J. Waringa, *TAPPI PLACE Conference*, Indianapolis, USA 32 (2004).
18. O. Mahdaoui, P. Laure, and J.-F. Agassant, *J. Non-Newton. Fluid Mech.*, **195**, 67 (2013).
19. L.C. Mendes, P.S.C. Pereira, and V.D. Ramos, *Macromol. Symp.*, **299**, 183 (2011).
20. V. Tanrattanakul, A. Hiltner, E. Baer, W.G. Perkins, F.L. Massey, and A. Moet, *Polymer*, **38**, 4117 (1997).
21. B. Khomami, *J. Non-Newton. Fluid Mech.*, **37**, 19 (1990).
22. J. Dooley and L. Dietsche, *Plast. Eng.*, **52**, 37 (1996).
23. P. Yue, C. Zhou, J. Dooley, and J.J. Feng, *J. Rheol.*, **52**, 1027 (2008).
24. E. Mitsoulis and F.L. Heng, *J. Appl. Polym. Sci.*, **34**, 1713 (1987).
25. A.E. Everage Jr., *Trans. Soc. Rheol.*, **17**, 629 (1973).
26. M.C. Williams, *AIChE. J.*, **21**, 1204 (1975).
27. C.D. Han, *J. Appl. Polym. Sci.*, **17**, 1289 (1973).
28. J.H. Southern and R.L. Ballman, *J. Appl. Polym. Sci.*, **20**, 175 (1973).
29. J.H. Southern and R.L. Ballman, *J. Polym. Sci.*, **13**, 863 (1975).
30. B.-L. Lee and J.L. White, *Trans. Soc. Rheol.*, **18**, 467 (1974).
31. C.D. Han, *Multiphase Flow in Polymer Processing*, Academic Press, New York (1981).
32. J. Dooley and L. Rudolph, *J. Plast. Film Sheet.*, **19**, 111 (2003).
33. K. Lamnawar, M. Bousmina, and A. Maazzouz, *Macromolecules*, **45**, 441 (2012).
34. G.M. Wilson and B. Khomami, *J. Non-Newton. Fluid Mech.*, **45**, 355 (1992).
35. J. Dooley, K.S. Hyun, and K. Hughes, *Polym. Eng. Sci.*, **38**, 1060 (1998).
36. J.L. White, R.C. Ufford, K.R. Dharod, and R.L. Price, *J. Appl. Polym. Sci.*, **16**, 1313 (1972).
37. B. Debbaut, T. Avalosse, J. Dooley, and K. Hughes, *J. Non-Newton. Fluid Mech.*, **69**, 255 (1997).
38. J. Dooley and L. Rudolph, *TAPPI PLACE Conference* (2002).
39. J. Dooley, *TAPPI PLACE Conference* (2004).
40. J. Dooley, *TAPPI PLACE Conference* (2007).
41. J. Dooley, C. Costeux, R. Wrisley, and A. Schadler, *TAPPI PLACE Conference* (2008).
42. H. Mavridis, A.N. Hrymak, and J. Vlachopoulos, *AIChE. J.*, **33**, 410 (1987).
43. A. Karagiannis, A.N. Hrymak, and J. Vlachopoulos, *Rheol. Acta*, **29**, 71 (1990).
44. W.A. Gifford, *Polym. Eng. Sci.*, **37**, 315 (1997).
45. M. Gupta, *ANTEC*, **56**, 2030 (2010).
46. M. Gupta, *ANTEC*, **58** (2012).
47. G. Sornberger, B. Vergnes, and J.F. Agassant, *Polym. Eng. Sci.*, **26**, 455 (1986).
48. A. Karagiannis, H. Mavridis, A.N. Hrymak, and J. Vlachopoulos, *Polym. Eng. Sci.*, **28**, 982 (1988).
49. C.D. Han, *J. Appl. Polym. Sci.*, **19**, 1875 (1975).
50. A. Torres, A.N. Hrymak, J. Vlachopoulos, J. Dooley, and B.T. Hilton, *Rheol. Acta.*, **32**, 513 (1993).
51. T.I. Butler, *TAPPI* 205 (1992).
52. A. Rincon, J. Ulcej, and D. Pitsch, *TAPPI PLACE Conference* (2002).
53. H. Helmy, *Adv. Polym. Tech.*, **7**, 59 (1987).
54. H. Helmy, *J. Plast. Film Sheet.*, **4**, 193 (1987).
55. A. Karagiannis, A.N. Hrymak, and J. Vlachopoulos, *Rheol. Acta.*, **28**, 121 (1989).
56. K.B. Sunwoo, S.J. Park, S.J. Lee, K.H. Ahn, and S.J. Lee, *Korea-Aust. Rheol. J.*, **12**, 165 (2000).
57. B.K. Carter, R.L. Lucking, J.A. Klein, and S.J. Israel, U.S. Patent 5,759,467 (1998).
58. J.A. Klein, B.K. Carter, S.J. Israel, and R.L. Lucking, U.S. Patent 5,783,283 (1998).
59. E.A. Grulke, *Polymer Process Engineering*, PTR Prentice Hall, New Jersey (1994).
60. S.A. Jabarin and E.A. Lofgren, *Polym. Eng. Sci.*, **24**, 1056 (1984).
61. K.B. Sunwoo, S.J. Park, S.J. Lee, K.H. Ahn, and S.J. Lee, *J. Non-Newton. Fluid Mech.*, **99**, 125 (2001).
62. S.J. Park, K.H. Ahn, and S.J. Lee, *Korea-Aust. Rheol. J.*, **13**, 37 (2001).
63. C.W. Hirt and B.D. Nichols, *J. Comput. Phys.*, 201 (1981).
64. J.C. Vickerman and D. Briggs, *TOF-SIMS: Surface Analysis by Mass Spectrometry*, 2nd ed., IM Publications LLP, London (2013).
65. J. Champion, M.K. Looney, and M.J.H. Simmons, *TAPPI PLACE Conference* (2013).
66. P.D. Anderson, J. Dooley, and H.E.H. Meijer, *Appl. Rheol.*, **16**, 198 (2006).
67. D. Silagy, Y. Demay, and J.F. Agassant, *Int. J. Numer. Meth. Fl.*, **30**, 1 (1999).
68. C. Sollogoub, Y. Demay, and J.F. Agassant, *Int. Polym. Proc.*, **18**, 80 (2003).